A frequency domain finite element solver for acoustic simulations of 3D rooms with microperforated panel absorbers

Okuzono, Takeshi

Sakagami, Kimihiro

(Citation)
Applied Acoustics,129:1-12

(Issue Date)
2018-01

(Resource Type)
journal article

(Version)
Accepted Manuscript

A frequency domain finite element solver for acoustic simulations of 3D rooms with microperforated panel absorbers

Takeshi Okuzono[a,1] Kimihiro Sakagami[a]

[a]*Environmental Acoustic Laboratory, Department of Architecture, Graduate School of Engineering, Kobe University, 1-1, Rokkodai-cho, Nada-ku, Kobe-city 657-8501, Japan*

Abstract

Microperforated panel (MPP) absorbers, which provide broadband sound absorption without the use of fibrous materials, have favorable material properties that support recyclability, flexibility of design, hygiene demands, and cleaning. Many earlier studies have specifically examined the development of absorbers themselves. However, to use the absorption performance of MPP absorbers sufficiently in room acoustic applications, it is beneficial to develop accurate prediction methods of sound fields in rooms with MPP absorbers. Such methods are expected to be useful for room acoustics design and absorber design tools. This study constructs a frequency domain finite element (FE) solver for acoustic simulations of a practical sized room with MPP absorbers. Then the accuracy and effectiveness are evaluated. In the FE solver, spatial domains are discretized by fourth-order accurate FEs in terms of dispersion error, and MPP absorbers are modeled using first-order hexahedral limp MPP elements that can deal with sound propagation in the backing structure of absorbers. First, the accuracy of present FE solver is demonstrated using impedance tube problems in comparison with conventional second-order accurate FEs. Results show higher convergence of solutions for the present FE solver. Then, exploration of an iterative solver for efficient multi-frequency analyses reveals that the recently developed CSQ-MOR is a faster and more stable solver. Finally, comparison with a con-

[1]Corresponding author. Tel./fax: +81 78 803 6577.
E-mail address: okuzono@port.kobe-u.ac.jp (T. Okuzono).

ventional surface impedance model based on a locally reacting assumption confirms the effectiveness of present FE solver by presenting the importance of dealing with the incident angle dependence of reactance of a rigid-backed air cavity in the modeling of single-leaf MPP absorbers.

Keywords: Room acoustics, Microperforated panel, Finite element method, Frequency domain, Absorption

1. Introduction

Sound absorbers play an important role in controlling reverberation and improving speech intelligibility in rooms. Various absorbers include porous absorbers, plate/membrane type absorbers, and Helmholtz resonators, each having their unique absorption characteristics. A microperforated panel (MPP) is a thin panel with submillimeter perforations. The panels are made out of arbitrary materials such as metal and plastic. Actually, MPP absorbers have received considerable attention in recent years because they have more broadband sound absorption than conventional perforated panel absorbers, without the use of porous materials. They also have great value from perspectives of recyclability, designability, hygiene demands, and cleaning. Various MPP absorbers have been developed with these attractive features. The typical configuration is placing an MPP in front of a rigid backed air cavity to form a Helmholtz resonator [1, 2]. However, the absorption characteristics show frequency-selective behaviors. Additionally, its bandwidth with high absorption is not so wide for general purpose absorbers. For these reasons, many studies have been conducted to broaden the absorption bandwidth [1, 3, 4, 5, 6, 7, 8]. Multi-layer constructions [1, 3, 5, 6] and the parallel arrangement of MPP absorbers with different cavity depths [4, 7, 8] exemplify such wideband MPP absorbers.

However, to use the absorption performance of MPP absorbers sufficiently or to use them appropriately in room acoustic applications, it is beneficial to develop accurate prediction methods of sound fields in rooms with MPP absorbers based on wave acoustics. For example, installing absorbing materials in rectangular rooms such as classrooms and offices frequently engenders non-diffuse sound fields. It is difficult to predict such sound fields using a diffuse field theory such as Sabine and Eyring reverberation formulas [9, 10]. In such a non-diffuse sound field, wave-based prediction methods such as finite element method (FEM) can be useful to explore the optimum sound absorber

location. Furthermore, the development of accurate wave-based methods enables us to evaluate the absorption performance of MPP absorbers in actual installed conditions. That is useful to elucidate in-situ absorption performance of MPP absorbers and to develop further high-performance MPP absorbers.

In wave-based methods, a surface impedance model based on the assumption of local reaction is usually used to model absorbers simply. However, that model might produce inaccurate results when surface impedance of absorbers depends strongly on incidence angles. In such cases, a proper absorber model that can deal with frequency and incident angle dependence of surface impedance i.e., an extended reacting model, is necessary for accurate sound field analyses. Such a model can be constructed by dealing with sound propagation inside absorbers. Although wave-based predictions of sound fields in practical sized rooms with the appropriate absorber model have been regarded as difficult because of their high computational cost, recent advances in computer technology present the possibility of such prediction [11, 12].

Recently, the authors presented a frequency domain finite element (FE) formulation for acoustics simulations of rooms with MPP absorbers [11]. In that formulation, MPP itself is assumed as a locally reacting material because MPP is too thin, but sound propagation in the backing structure can be treated appropriately by introducing boundary conditions in both MPP surfaces. Therefore, the absorption model is the extended reacting model, with validity shown through two-dimensional numerical experiments based on an impedance tube method for measuring normal incidence absorption characteristics. This study also presented theoretical memory requirements for three-dimensional analyses, which revealed that sound field predictions of practical sized rooms are within the scope of analyses. However, the FE formulation has not yet been applied to three-dimensional analyses and calculations of transient responses, which are important for room acoustic applications.

As described in this paper, a frequency domain FE solver for acoustic simulations of 3D room with MPP absorbers is developed. The purpose of this paper is to show the accuracy and effectiveness. First, first-order eight-node hexahedral MPP elements are derived for modeling MPP absorbers in three-dimensional analyses. Detailed discretization procedures to solve sound fields in rooms are also presented, including the explanation of fourth-order accurate eight-node hexahedral FEs for spatial discretization. Secondly, the

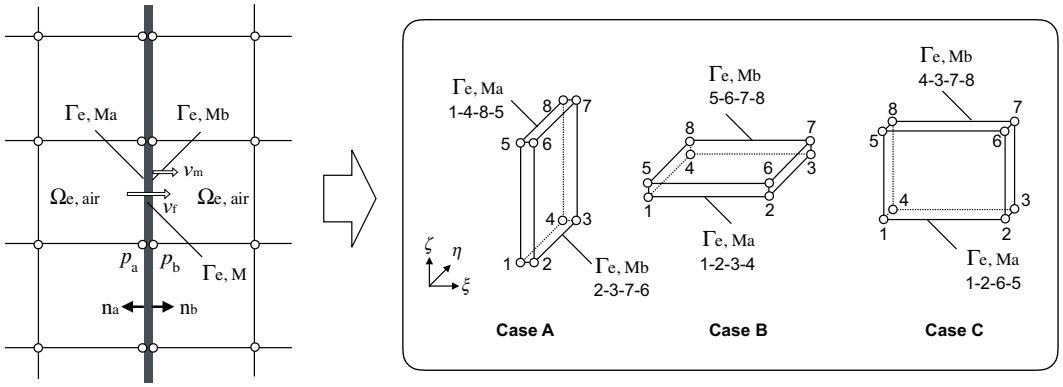

(a) FE model of MPP

(b) Three cases of eight node hexahedral MPP elements

Figure 1: FE model of MPP (a) and eight-node hexahedral MPP elements in three cases (b).

accuracy is shown through impedance tube problems. Then, a proper iterative solver is explored for performing multi-frequency analyses efficiently. Finally, the importance of dealing with the incident angle dependence of surface impedance is demonstrated to underscore the effectiveness of the present FE solver. An earlier report of the literature [13] presents the importance as preliminary results for two-dimensional steady-state sound fields. The presented paper provides more detailed discussion related to three-dimensional analyses including transient sound fields.

2. Theory

2.1. FE model of MPP

In the present MPP elements, an MPP is assumed as limp. The effect of microperforation is modeled using Maa's impedance model [1]. Two material parameters are used to construct the elements: the surface density M_{MPP} and acoustic impedance Z_{MPP} of MPP. The resulting matrix expression of MPP elements is also presented explicitly for convenience.

Figures 1(a) and 1(b) present an FE model of an MPP and three cases of eight-node hexahedral MPP elements with different absorbing surfaces, where $\Omega_{\mathrm{e,air}}$ and $\Gamma_{\mathrm{e,M}}$ represent the air element and MPP element derived with contribution from both boundary surfaces of MPP $\Gamma_{\mathrm{e,Ma}}$ and $\Gamma_{\mathrm{e,Mb}}$. In addition, p_{a} and p_{b} represent the sound pressures at both sides of MPP. In

addition, v_f and v_m represent the average particle velocity over a tube cross-section and vibration velocity of MPP. $\mathbf{n}_\mathrm{a}$ and $\mathbf{n}_\mathrm{b}$ are the normal vectors at the boundaries. As presented in Fig. 1(b), the three cases with different absorbing surfaces exist in the MPP elements for three-dimensional analyses. For example, in Case A, the absorbing surfaces of MPP, $\Gamma_\mathrm{e,Ma}$ and $\Gamma_\mathrm{e,Mb}$ respectively consist of nodes 1–4–8–5 and 2–3–7–6, where the number is element node numbers in the local coordinate (ξ, η, ζ) system. Considering cases A–C in the MPP elements is important for implementation because locations of element components in the resulting matrix differ among the cases.

2.2. Boundary conditions of MPP surfaces

Regarding boundary conditions of MPP, a vibration boundary is assumed in the boundary surfaces of the MPP element $\Gamma_\mathrm{e,Ma}$ and $\Gamma_\mathrm{e,Mb}$, as described below.

$$\frac{\partial p}{\partial n} = \begin{cases} -i\omega\rho_0(v_\mathrm{m} + v_\mathrm{f}) & \text{on } \Gamma_\mathrm{e,Ma}, \\ i\omega\rho_0(v_\mathrm{m} + v_\mathrm{f}) & \text{on } \Gamma_\mathrm{e,Mb}. \end{cases} \tag{1}$$

Therein, i, ω, and ρ_0 respectively represent the imaginary unit, angular frequency, and air density. In this formulation, MPP itself is modeled as a locally reacting material because MPP is too thin, having less than 1 mm thickness. However, by introducing the boundary conditions into both surfaces of MPP, a sound field in rooms is coupled to a field in a backing structure of MPP. Therefore, the presented formulation can deal with sound propagation in the backing structure of MPP.

The vibration velocity v_m in Eq. (1) is calculable using the equation of motion for a limp MPP, which is given as

$$i\omega M_\mathrm{MPP} v_\mathrm{m} = p_\mathrm{a} - p_\mathrm{b}. \tag{2}$$

The particle velocity v_f is obtainable from the following definition of the acoustic impedance of MPP

$$Z_\mathrm{MPP} = \frac{p_\mathrm{a} - p_\mathrm{b}}{v_\mathrm{f}}. \tag{3}$$

The effect of microperforation is modeled by Maa's impedance model. The acoustic impedance of MPP including end corrections is given approximately as [1]

$$Z_\mathrm{MPP} = \frac{R_0 + iX_0}{\sigma}, \tag{4}$$

Table 1: Shape function of eight-node hexahedral MPP elements for Case A, in which absorbing surfaces of MPP, $\Gamma_{\mathrm{e,Ma}}$ and $\Gamma_{\mathrm{e,Mb}}$, consist respectively of nodes 1–4–8–5 and 2–3–7–6.

	i=1, 2	i=4, 3	i=8, 7	i=5, 6
N_i	$\frac{1}{4}(1-\eta)(1-\zeta)$	$\frac{1}{4}(1+\eta)(1-\zeta)$	$\frac{1}{4}(1+\eta)(1+\zeta)$	$\frac{1}{4}(1-\eta)(1+\zeta)$
$\frac{\partial N_i}{\partial \eta}$	$-\frac{1}{4}(1-\zeta)$	$\frac{1}{4}(1-\zeta)$	$\frac{1}{4}(1+\zeta)$	$-\frac{1}{4}(1+\zeta)$
$\frac{\partial N_i}{\partial \zeta}$	$-\frac{1}{4}(1-\eta)$	$-\frac{1}{4}(1+\eta)$	$\frac{1}{4}(1+\eta)$	$\frac{1}{4}(1-\eta)$

with

$$R_0 = \frac{32\eta t}{d^2}\left(\sqrt{1+\frac{K^2}{32}} + \frac{\sqrt{2}}{8}K\frac{d}{t}\right), \tag{5}$$

$$X_0 = \rho_0 \omega t\left(1 + \frac{1}{\sqrt{9+\frac{K^2}{2}}} + 0.85\frac{d}{t}\right), \tag{6}$$

$$K = d\sqrt{\frac{\omega\rho_0}{4\eta}}, \tag{7}$$

where t, d, σ, and η respectively denote the panel thickness, hole diameter, perforation ratio, and dynamic viscosity of the air (17.9 μPa s).

2.3. Eight-node hexahedral MPP elements

Before presenting the detailed FE discretization procedure of a closed steady state sound field with MPP, we show the derivation of first-order eight-node hexahedral MPP elements for three-dimensional analyses. In the discretization procedure, contributions from both boundary surfaces of MPP, i.e., $\Gamma_{\mathrm{e,Ma}}$ and $\Gamma_{\mathrm{e,Mb}}$, are expressed as

$$\int_{\Gamma_{\mathrm{e,M}}} \boldsymbol{N}^{\mathrm{T}} \frac{\partial p}{\partial n} dA = \int_{\Gamma_{\mathrm{e,Ma}}} \boldsymbol{N}^{\mathrm{T}} \frac{\partial p}{\partial n} dA + \int_{\Gamma_{\mathrm{e,Mb}}} \boldsymbol{N}^{\mathrm{T}} \frac{\partial p}{\partial n} dA, \tag{8}$$

where $\boldsymbol{N}$ and dA respectively represent the shape function and area integral. With the boundary conditions of Eq. (1), the terms in right-hand side of Eq. (8) are given respectively as

$$\int_{\Gamma_{\mathrm{e,Ma}}} \boldsymbol{N}^{\mathrm{T}} \frac{\partial p}{\partial n} dA = -\left(\frac{\rho_0}{M_{\mathrm{MPP}}} + \frac{i\omega\rho_0}{Z_{\mathrm{MPP}}}\right) \int_{\Gamma_{\mathrm{e,Ma}}} \boldsymbol{N}_{\mathrm{a}}^{\mathrm{T}} (\boldsymbol{N}_{\mathrm{a}} - \boldsymbol{N}_{\mathrm{b}}) dA \boldsymbol{p}_{\mathrm{e}}, \tag{9}$$

$$\int_{\Gamma_{\mathrm{e,Mb}}} \boldsymbol{N}^{\mathrm{T}} \frac{\partial p}{\partial n} dA = \left(\frac{\rho_0}{M_{\mathrm{MPP}}} + \frac{i\omega\rho_0}{Z_{\mathrm{MPP}}}\right) \int_{\Gamma_{\mathrm{e,Mb}}} \boldsymbol{N}_{\mathrm{b}}^{\mathrm{T}} (\boldsymbol{N}_{\mathrm{a}} - \boldsymbol{N}_{\mathrm{b}}) dA \boldsymbol{p}_{\mathrm{e}}. \tag{10}$$

Here, $\boldsymbol{N}_{\mathrm{a}}$ and $\boldsymbol{N}_{\mathrm{b}}$ respectively represent the shape functions at nodes on $\Gamma_{\mathrm{e,Ma}}$ and $\Gamma_{\mathrm{e,Mb}}$. The same shape function as first-order air elements is used for the geometry and sound pressure. Table 1 presents the shape function for eight-node hexahedral MPP elements for Case A in Fig. 1(b). For Cases B and C, the shape functions are obtained respectively by replacing η and ζ with ξ and η (Case B), and by replacing η and ζ with ξ and ζ (Case C), along the corresponding axis in the local coordinate system. In addition, for Case B, the corresponding nodal pair changes to $i = 1, 5$, $i = 2, 6$, $i = 3, 7$, and $i = 4, 8$ from the left side in Table 1, and $i = 1, 4$, $i = 2, 3$, $i = 6, 7$, and $i = 5, 8$ in Case C.

Using two-dimensional Gauss quadrature rules with two integration points at each direction, the element matrix $\boldsymbol{D}_{\mathrm{e}}$ of the first-order MPP elements for Case A is given as

$$\boldsymbol{D}_{\mathrm{e}} = \frac{S_{\mathrm{e}}}{36}\left(\frac{1}{M_{\mathrm{MPP}}} + \frac{i\omega}{Z_{\mathrm{MPP}}}\right) \begin{bmatrix} 4 & -4 & -2 & 2 & 2 & -2 & -1 & 1 \\ -4 & 4 & 2 & -2 & -2 & 2 & 1 & -1 \\ -2 & 2 & 4 & -4 & -1 & 1 & 2 & -2 \\ 2 & -2 & -4 & 4 & 1 & -1 & -2 & 2 \\ 2 & -2 & -1 & 1 & 4 & -4 & -2 & 2 \\ -2 & 2 & 1 & -1 & -4 & 4 & 2 & -2 \\ -1 & 1 & 2 & -2 & -2 & 2 & 4 & -4 \\ 1 & -1 & -2 & 2 & 2 & -2 & -4 & 4 \end{bmatrix}, \tag{11}$$

where S_{e} is the area of an absorbing surface.

2.4. Discretization of sound field

We consider a closed sound field Ω_{f} with a boundary Γ governed by the nonhomogeneous wave equation expressed in sound pressure p as

$$\frac{\partial^2 p}{\partial^2 t} - c_0^2 \nabla^2 p = \rho_0 c_0^2 \frac{\partial q}{\partial t}, \tag{12}$$

where c_0 and q represent the speed of sound and added fluid mass per unit volume. ∇ denotes the gradient of a variable. The weak form of nonhomogeneous wave equation for finite element discretization is

$$\int_{\Omega_{\mathrm{f}}} \phi \frac{\partial^2 p}{\partial^2 t} dV + c_0^2 \int_{\Omega_{\mathrm{f}}} \nabla\phi \nabla p dV = c_0^2 \int_{\Gamma} \phi \frac{\partial p}{\partial n} dA + \rho_0 c_0^2 \int_{\Omega_{\mathrm{f}}} \phi \frac{\partial q}{\partial t} dV, \tag{13}$$

where ϕ and dV respectively represent the arbitrary weight function and volume integral. Introducing finite element approximations to the sound pressure and the weight function gives

$$\sum_{e}^{n_{\mathrm{e}}}\left[\int_{\Omega_{\mathrm{e}}}\nabla \boldsymbol{N}^{T}\nabla \boldsymbol{N}dV\boldsymbol{p}_{\mathrm{e}}-k^{2}\int_{\Omega_{\mathrm{e}}}\boldsymbol{N}^{T}\boldsymbol{N}dV\boldsymbol{p}_{\mathrm{e}}-\int_{\Gamma_{\mathrm{e}}}\boldsymbol{N}^{T}\frac{\partial p}{\partial n}dA\right]=\sum_{e}^{n_{\mathrm{e}}}\left[i\omega\rho_{0}\int_{\Omega_{\mathrm{e}}}\boldsymbol{N}^{T}qdV\right]. \tag{14}$$

Here, the time factor $e^{i\omega t}$ is assumed with the angular frequency ω. The symbols k, $\boldsymbol{p}_{\mathrm{e}}$, n_{e}, Ω_{e}, and Γ_{e} represent the wave number, nodal sound pressure vector, number of FEs, region of an FE and boundary of an FE. Inserting four boundary conditions for rigid boundary, vibrating boundary, impedance boundary, and MPP boundary yields

$$[\boldsymbol{K}-k^{2}\boldsymbol{M}+ik\boldsymbol{C}+\rho_{0}\boldsymbol{D}]\boldsymbol{p}=\boldsymbol{f}, \tag{15}$$

where $\boldsymbol{K}$, $\boldsymbol{M}$, $\boldsymbol{C}$, and $\boldsymbol{D}$ respectively represent the global stiffness matrix, global mass matrix, global dissipation matrix, and the global matrix of MPP element. Furthermore, $\boldsymbol{p}$ and $\boldsymbol{f}$ respectively denote the sound pressure vector and external force vector. The sound pressure is calculated by solving the linear system of equations at a wavenumber k with a linear equation solver. The coefficient matrix is a sparse complex symmetric matrix with an extremely small percentage of nonzero entries. It is important to exploit the matrix property for the efficient solution.

The two types of linear equation solvers are direct solvers, such as LU decomposition, and iterative solvers, such as conjugate gradient method. For large-scale analyses, iterative solvers are efficient from the perspective of memory requirements because they can solve a linear system of equations by storing only nonzero entries. An efficient iterative solver for Eq. (15) is presented in Section 4.

2.5. FEs for spatial discretization and its dispersion error property

For spatial discretization we use eight-node hexahedral linear elements with modified integration rules [14] (MIR) to reduce dispersion errors. Using the elements, the overall degrees of freedom can be reduced considerably compared to conventional first-order elements with second-order accuracy, to achieve an equal level of accuracy. Dispersion errors, an inherent error of FEM, derive from spatial discretization. It is defined as the difference between the exact wavenumber k and approximate wavenumber k^{h}. In spite

of first-order elements, the element with MIR has fourth-order accuracy with respect to dispersion errors. Dispersion errors can be estimated theoretically in an idealized case, i.e., a plane wave propagation in a free space that uses a uniformly discretized mesh by rectangular elements. For three-dimensional analyses, the dispersion error for the FEs with MIR is given as

$$\left|\frac{k-k^h}{k}\right| = \frac{k^4}{480}|d_x^4 \sin^6\theta\cos^6\phi + d_y^4 \sin^6\theta\sin^6\phi + d_z^4\cos^6\theta|, \tag{16}$$

where d_x, d_y, and d_z respectively represent the element length of rectangular element in x, y, and z directions. In addition, θ and ϕ respectively denote the elevation and azimuth in a spherical coordinate system.

However, the dispersion error for conventional eight-node hexahedral linear elements is

$$\left|\frac{k-k^h}{k}\right| = \frac{k^2}{24}|d_x^2 \sin^4\theta\cos^4\phi + d_y^2 \sin^4\theta\sin^4\phi + d_z^2\cos^4\theta|. \tag{17}$$

To demonstrate the accuracy of MIR, the relation between the spatial resolutions of FE mesh and dispersion errors calculated using Eqs. (16) and (17) are presented for comparison in Fig. 2, where the spatial resolution means number of elements per wavelength. In the calculation, d_x, d_y, and d_z are set to 0.05 m, and the errors are calculated in a direction (θ, ϕ) = (90°, 90°), at which the maximum error occurs. For both elements, the maximum error occurs in an axial direction with longest element size. The conventional FEs have 1.64% error at the well known rule of thumb, i.e., 10 elements per wavelength; it needs approximately 12.8 elements to maintain the error within 1.0%. The FEs with MIR achieve the error level of 1.0% at the 4.25 elements per wavelength.

3. Impedance tube problems

To show the accuracy and convergence of solutions of present FE solver, impedance tube problems with single-leaf MPP absorbers were used as a benchmark problem. Using three FE meshes with different spatial resolutions, the surface impedance and absorption coefficient of the absorbers were calculated directly from a sound pressure and a particle velocity on the absorber surface. Then they were compared with those calculated using the

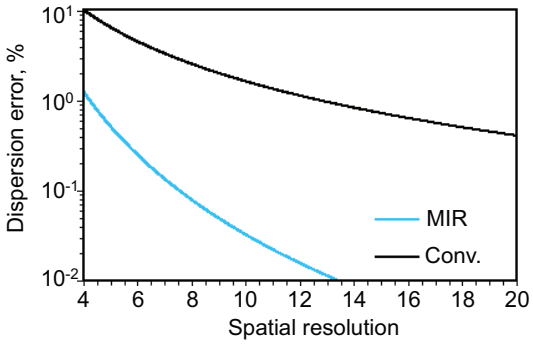

Figure 2: Comparison of dispersion errors between eight-node hexahedral FEs using MIR and conventional FEs.

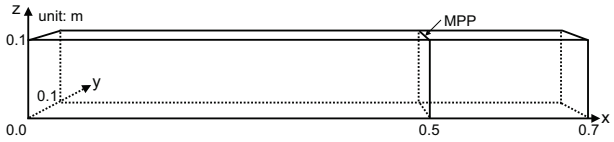

Figure 3: Impedance tube problem with a single-leaf MPP absorber.

electro-acoustical equivalent circuit theory [15]. Calculations using the conventional second-order accurate FEs were also performed to show the superiority of using MIR. Figure 3 shows the impedance tube with the single-leaf MPP absorber. Two MPPs with different material parameters were, respectively, installed with a rigid-backed air cavity of 0.2 m depth: (1) MPP1 of $d = 0.2$ mm, $t = 0.18$ mm, $\sigma = 0.6\%$, $M_{\mathrm{MPP}} = 0.6$ kg/m^2; and (2) MPP2 of $d = 0.15$ mm, $t = 1.0$ mm, $\sigma = 1.0\%$, $M_{\mathrm{MPP}} = 1.2$ kg/m^2. Vibration acceleration of 1.0 m^3/s^2 was given on a surface in the left-hand side of tube end. The remaining boundaries were assumed to be rigid. Calculations were performed at frequencies of 20 Hz to 1.5 kHz with 1 Hz interval. The spatial resolutions of three FE meshes are, respectively, 4.58 (Mesh 1), 9.17 (Mesh 2) and 18.3 (Mesh 3) elements per wavelength at the upper-limit frequency.

Figures 4(a) and 4(b) respectively show absorption coefficients of the MPP absorbers with MPP1 and MPP2 calculated using the theory and present FE solver without (Conv.) and with MIR (MIR) for Mesh 1 – Mesh 3. For both the MIR and Conv. the results of Mesh 2 and Mesh 3 overlapped well with the theory. The discrepancies from theory are visible only for the results of Mesh 1. For MIR, discrepancies are observed around 1.5 kHz, but the discrepancies for Conv. appear from around second peak fre-

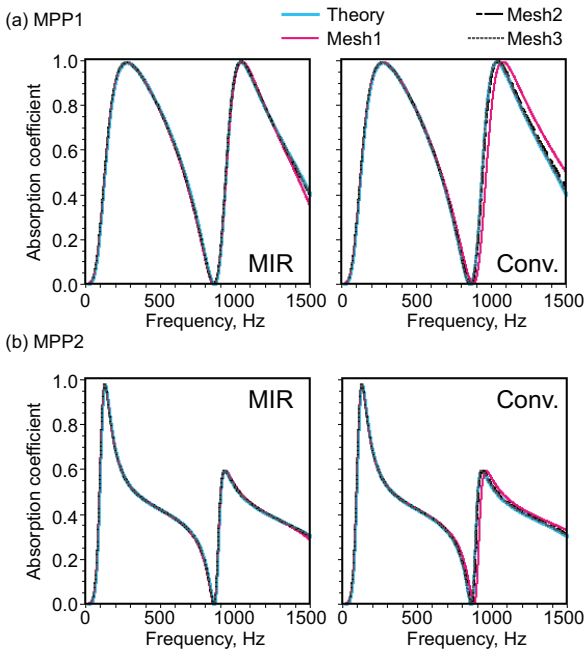

Figure 4: Theoretical absorption coefficients versus those calculated using present FE solver with MIR (left) and with conventional FEs (right) for Mesh1∼3: (a) MPP1 and (b) MPP2.

quencies. Table 2 presents the second peak frequencies of MIR and Conv. for Mesh 1 – Mesh 3, and the relative errors from theoretical second peak frequencies. For both the MIR and Conv. the numerical second peak frequencies converge to the theoretical frequencies using the finer mesh, and Mesh 1 of MIR produces more accurate results than Mesh 2 of Conv., which has spatial resolution close to the well known rule of thumb. The surface impedance of theory, MIR and Conv. are presented in Fig. 5 for MPP1. The results are presented only for Mesh 1 because the surface impedance of Mesh 2 and Mesh 3 is overlapped well with the theory. For MIR and Conv., discrepancies from theory can be found in only the reactance of impedance. For MIR, the discrepancy is only visible around 1.5 kHz, but the discrepancy for Conv., appears from lower frequencies. From the perspective of modeling of single-leaf MPP absorbers, it indicates that the influence of dispersion errors using a coarse mesh appears as the reduction of approximation accuracy in reactance of a rigid-backed air cavity. This becomes a problem if precise absorption characteristics of absorbers are necessary because the reactance

Table 2: Second peak frequency of MIR and Conv. for Mesh1∼3, and relative error from theoretical frequency. The theoretical second peak frequencies are, respectively, 1039 Hz and 931 Hz for MPP1 and 2.

	Mesh	MIR	Conv.
MPP1	1	1047 Hz (0.77%)	1080 Hz (3.95%)
	2	1041 Hz (0.19%)	1049 Hz (0.96%)
	3	1040 Hz (0.10%)	1042 Hz (0.29%)
MPP2	1	934 Hz (0.32%)	961 Hz (3.22%)
	2	932 Hz (0.11%)	938 Hz (0.75%)
	3	931 Hz (0.00%)	933 Hz (0.21%)

of a rigid-backed air cavity plays an important role in determining the peak and notch frequencies of single-leaf MPP absorbers. The accuracy of MIR is evaluated further using the 1/3 oct. band RMS error between the theoretical absorption coefficient $\alpha_{\mathrm{Theory}}(f)$ and numerical absorption coefficient $\alpha_{\mathrm{FEM}}(f)$ defined as

$$\alpha_{\mathrm{rms}} = \sqrt{\frac{1}{N_{\mathrm{f}}} \sum_{f=f_{\mathrm{l}}}^{f_{\mathrm{u}}} [\alpha_{\mathrm{FEM}}(f) - \alpha_{\mathrm{Theory}}(f)]^2}, \tag{18}$$

where N_{f}, f_{l} and f_{u} respectively represent the number of frequencies including 1/3 oct. band, lower and upper limit frequencies of 1/3 oct. band. Figures 6(a) and 6(b), respectively show comparisons of the RMS errors of MIR and Conv. for MPP1 and MPP2, which was calculated for Mesh 1 – Mesh 3. Results show that MIR is more accurate than Conv. for the mesh with the same spatial resolution. As expected from Fig. 2, the accuracy of MIR for Mesh1 is better than that of Conv. for Mesh 2 at higher frequencies, where dispersion errors have larger influence on the resulting accuracy. This engenders reduction in the degrees of freedom by about one-eighth.

From the results described above, it can be concluded that the solutions of the present FE solver with MIR converge with theoretical values using FE meshes of lower spatial resolution than those by conventional FEs.

4. Exploration of efficient iterative solver

In the use of frequency domain finite element simulations, a transient response is calculable using an indirect approach with inverse Fourier trans-

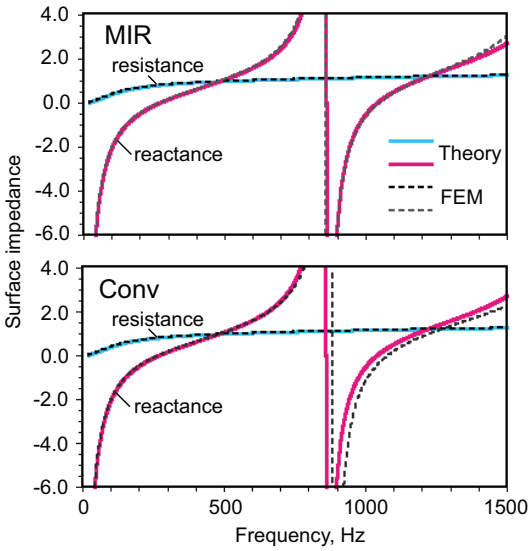

Figure 5: Surface impedances of theory, MIR and Conv. for MPP1 calculated using Mesh 1. (Upper) MIR, and (Lower) Conv.

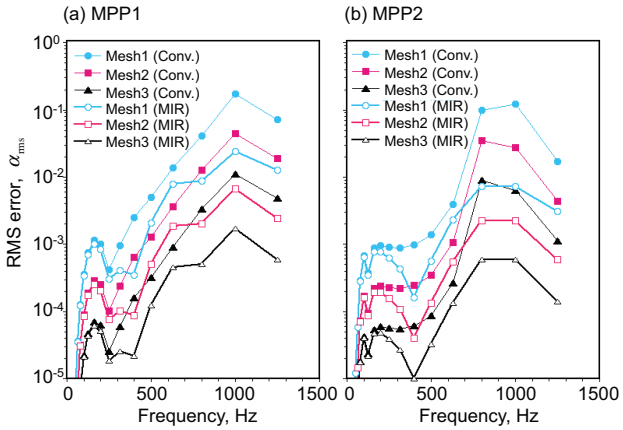

Figure 6: Comparison of RMS errors in absorption coefficients of MIR and Conv. calculated using Mesh 1 – Mesh 3: (a) MPP1 and (b) MPP2.

form. For such an approach, pure tone analyses at many frequencies i.e., multi-frequency analyses, are necessary to obtain a broad band transient response. For calculations of room acoustic parameters such as reverberation times, frequency intervals must be set to a value of the reciprocal of estimated reverberation times of rooms, at least. For example, as explained in the next

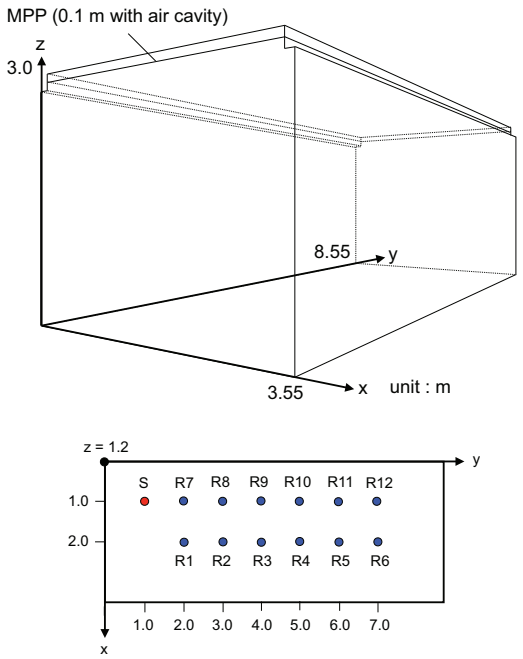

Figure 7: (Upper) A simulated room with volume of 91 m^3 in the case with MPP absorbers, where a single-leaf MPP absorber with 0.1 m air cavity is installed on the ceiling. (Lower) Source (S) and 12 receivers positions (R1–R12) located on a plane at $z = 1.2$ m.

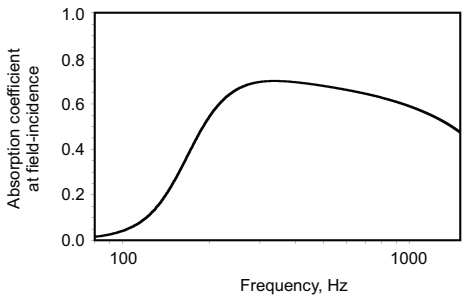

Figure 8: Field-incidence absorption coefficient of a single-leaf MPP absorber with a rigid backed air cavity of 0.1 m. The material parameters are $d = 0.15$ mm, $t = 1.0$ mm, $\sigma = 1.0\%$, and $M_{\mathrm{MPP}} = 1.2$ kg/m^2.

section, when an estimated reverberation time is 2.0 s, a frequency interval must be set to 0.5 Hz or less. Such calculations are extremely time-consuming because the linear system of equations must be solved at many frequencies. Therefore, the selection of efficient linear equation solver can have a marked

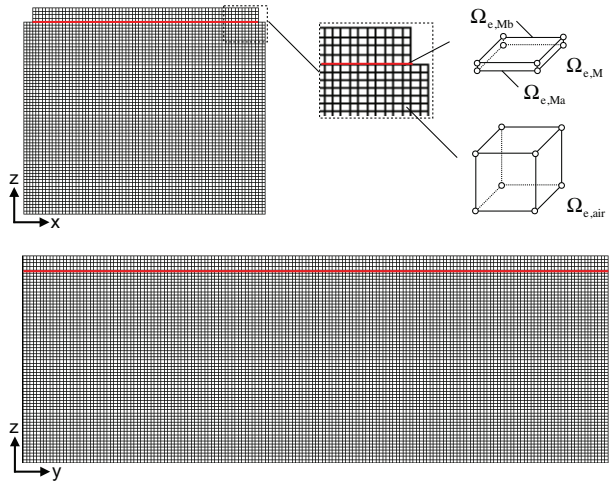

Figure 9: FE mesh for the case with MPP ceiling absorber, where z–x and y–z planes are shown. MPP elements in Case B are used.

impact on calculations of a transient response and room acoustical parameters in practical applications. The purpose of this section is to reveal an efficient iterative solver for the linear system of equations with complex symmetric matrix of Eq. (15).

For the use of iterative solvers, it is important to select a proper solver from various solvers because the performance is problem-dependent. In other words, the use of an inappropriate solver leads to slow convergence or even divergence. Regarding the selection of iterative solver suitable for room acoustic simulations using a frequency domain FEM, Okamoto et al. [16] compared the performance of four iterative solvers called COCG [17], CGS [18], BiCGStab [19], and GP-BiCG [20] with numerical experiments related to real-life problems. The results revealed COCG as an efficient solver for linear equations with complex symmetric matrix arise in the frequency domain FEM. However, there exist other iterative solvers for a complex symmetric matrix. No performance comparison for room acoustic simulations has yet been conducted sufficiently. Here, we conducted a performance comparison of four iterative solvers for complex symmetric matrices, including recently developed solvers.

4.1. Four iterative solvers for complex symmetric matrix

We applied four iterative solvers for a complex symmetric matrix: COCG, CSQMR [21], COCR [22], and CSQMOR [23]. In a recent study, both COCR

Table 3: Normalized surface impedance values z_{e}s and the corresponding statistical absorption coefficients α_{s}s for boundaries.

	125 Hz	250 Hz	500 Hz	1000 Hz
z_{e}	95.0	113.9	126.3	131.0
α_{s}	0.077	0.065	0.059	0.057

and CSQMR gave comparable or superior performance to that of COCG, with smoother convergence behavior for a complex symmetric linear system, deriving from 200 $\times$ 200 central difference discretization of Helmholtz equations [22]. In addition, CSQMOR, which is a recently developed QMR method based on coupled two-term biconjugate A-orthonormalization procedures, showed competitive or superior performance to COCG, CSQMR, and COCR for a linear system discretized by a standard five-point finite difference of Helmholtz equations in two dimensions [23]. These are the reasons for the selection.

In subsequent numerical experiments, an absolute diagonal scaling preconditioning is applied to the iterative solvers. With the preconditioning, the scaled coefficient matrix is expressed as

$$a'_{ij} = \frac{a_{ij}}{\sqrt{|a_{ii}|}\sqrt{|a_{jj}|}}, \tag{19}$$

where a_{ij} and a'_{ij} are the components of coefficient matrix $\boldsymbol{A}$ of Eq. (15) before and after the preconditioning. The following relative residual 2-norm is used as a stopping criterion to halt the iterations.

$$\frac{||\boldsymbol{A}\boldsymbol{p}_i - \boldsymbol{b}||_2}{||\boldsymbol{b}||_2} \leq 10^{-6} \tag{20}$$

Therein, $\boldsymbol{b}$ and $\boldsymbol{p}_i$ respectively represent the right-hand side vector of Eq. (15) and i-th solution vector on i-th iteration. In the criterion, a tolerance that determines the resulting accuracy of sound pressure was set to 10^{-6} as a sufficiently small value. All computations were performed using double precision floating point arithmetic on a SMP cluster (HA8000-tc/HT210; Hitachi Ltd.) having mainly two processors (2.7 GHz, 12 core, E5-2697 v2, Xeon; Intel Corp.) per node located at Kyushu University. The Intel Fortran compiler ver. 14 was used with the optimize option "-xAVX -openmp". The four iterative solvers were parallelized by OpenMP, and 8core was used

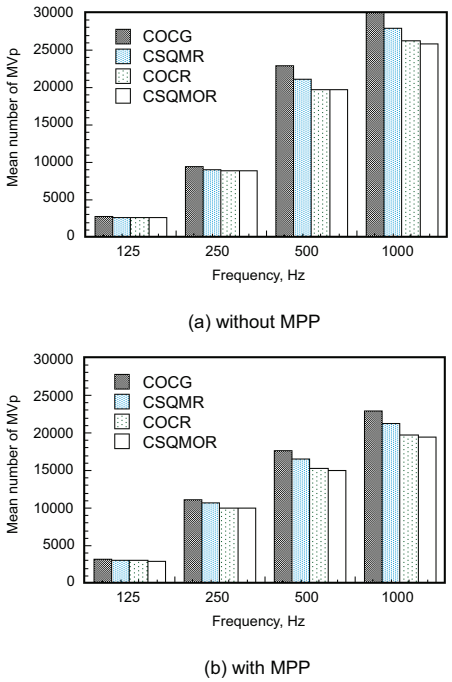

Figure 10: Mean number of MVp of four iterative solvers at 125 Hz, 250 Hz, 500 Hz, and 1000 Hz for cases (a) without MPP and (b) with MPP.

in the computations. Although the four solvers have different amounts of operation per iteration, the amounts of main operations are the same, i.e., single matrix-vector product (MVp) and two inner products. The number of MVp is used to evaluate the performance because it comprises a large percentage of operation in the iteration.

4.2. Simulated sound field and numerical setup

Sound fields of a rectangular room with reflective boundary surfaces are analyzed at low frequencies and medium frequencies in cases with and without MPP absorbers. Figure 7 depicts the simulated rectangular room in the case with a single-leaf MPP ceiling absorber with 0.1 m air cavity. Source and receiver positions are also presented in the lower part of Fig. 7. The point source S with volume acceleration of 1.0 m^3/s^2 is located at frequencies of 80 Hz to 1414 Hz with 1 Hz intervals. Sound pressures were calculated at the 12 receivers R1–R12. The material parameters of MPP are, respectively, $d =$ 0.15 mm, $t = 1.0$ mm, $\sigma = 1.0\%$, and $M_{\mathrm{MPP}} = 1.2$ kg/m^2. Figure 8 presents

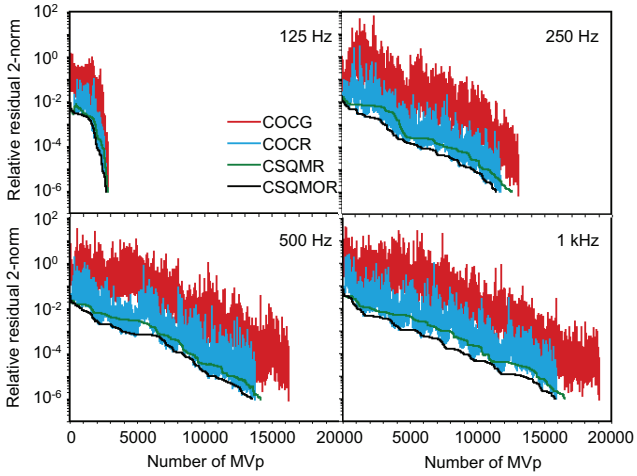

Figure 11: Relative residual 2-norm history of four iterative solvers at 125 Hz, 250 Hz, 500 Hz, and 1000 Hz for cases with MPP.

a field-incidence absorption coefficient of the single-leaf MPP absorber calculated using the electro-acoustical equivalent circuit theory [15]. For other boundaries, uniform real-valued surface impedance was given at each frequency. Table 3 presents the normalized surface impedance values z_es and the corresponding statistical absorption coefficients α_ss in Paris' formula. This section presents only the results of performance comparison among the four iterative solvers. Characteristics of sound fields with and without absorbers are presented in the next section.

As described above, FE meshes were created using the eight-node hexahedral elements with MIR and eight-node hexahedral MPP elements for air and MPP. With the spatial resolution of 4.9 elements per wavelength at 1414 Hz, the resulting DOFs of FE meshes in the cases with and without MPP are 876,225 and 864,150, respectively, for which a slight increase of DOF caused by the consideration of MPP is observed. Figure 9 is the FE mesh for the case with MPP ceiling absorber. Required memories in COCG, CSQMR, COCR, and CSQMOR were, respectively, 554 MB, 593 MB, 567 MB, and 607 MB for the case without MPP, and 562 MB, 602 MB, 575 MB, and 615 MB for the case with MPP. CSQMR and CSQMOR have more complicated algorithms than COCG or COCR. Therefore, these solvers require slightly more memory.

4.3. Performance comparison

Figures 10(a) and 10(b) present comparisons of mean number of MVp among the four iterative solvers at 125 Hz – 1 kHz for the cases without MPP and with MPP absorbers. The comparison is made using the mean value within an octave band of each center frequency. In both cases, the four iterative solvers require more iterations to achieve convergence at higher frequencies. The convergence behavior changes between low (125 Hz and 250 Hz) and mid-frequencies (500 Hz and 1 kHz). At the low frequencies, more iterations are necessary for the case with MPP, whereas the mid-frequency ranges require fewer iterations, indicating that the modeling of MPP absorber influences the convergence of iterative solvers. Moreover, the use of extended reacting model does not always engender a slow convergence. The fewer amounts of operation at mid-frequencies might derive from high absorption of the MPP absorber, as depicted in Fig. 8.

The performance comparison shows that the four solvers converge with almost identical iterations at the low frequencies. CSQMR, COCR, and CSQMOR give faster convergence than COCG at the mid-frequencies, and COCR and CSQMOR converge with fewer iterations than CSQMR. For COCR, the reductions of MVp relative to COCG are 13.5% and 13.8% at 500 Hz and 1 kHz for the case without MPP, and 13.6% and 13.7% for the case with MPP. CSQMOR has slightly increased values, which are 13.8% and 15.2% at 500 Hz and 1 kHz for the case without MPP, and 14.5% and 15.2% for the case with MPP. For CSQMOR the maximum value of reduction was 26.8%.

Figure 11 presents relative residual 2-norm histories of the four solvers at 125 Hz, 250 Hz, 500 Hz, and 1 kHz for the cases with MPP. Here, we omitted the results of the case without MPP because similar results were obtained. For the entire frequencies, the residual history of the four solvers shows similar tendencies. COCG converges with large fluctuations of the relative residual 2-norm. COCR also has large fluctuations, but the residual 2-norm is less than that of COCG at each iteration. In addition, CSQMR and CSQMOR converge monotonically without the fluctuation. The residual 2-norm of CSQMOR has smaller values than CSQMR and smallest values among the four solvers at most iteration step. This smaller residual 2-norm at each iteration of CSQMOR is important because it can also be expected to have faster convergence in the use of larger tolerance values in the stopping criterion. In practical applications, such situations arise frequently for a rough evaluation of sound field in rooms with reduced accuracy.

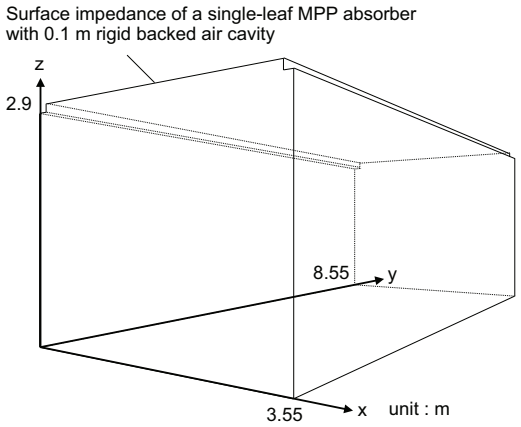

Figure 12: FE model for analyses with the surface impedance model. The rigid backed air cavity in Fig. 7 was removed.

The results above showed that CSQMOR is an efficient method with monotonic residual reduction and faster convergence for multi-frequency analyses using the present FE solver. It is especially effective at higher frequencies. In the next section, CSQMOR is used to compute transient responses in rooms.

5. Comparison of the presented FE solver with surface impedance model

This section presents the effectiveness of present FE solver in comparison with a conventional surface impedance model based on a locally reacting assumption. The effectiveness is shown by confirming the necessity of dealing with the incident angle dependence of surface impedance, in the modeling of single-leaf MPP absorbers. For that purpose, the sound field in rectangular room with MPP ceiling absorber of Fig. 7 is again analyzed at the low and medium frequencies. This sound field is an appropriate example because the resulting sound field becomes a non-diffuse sound field, as explained later. In non-diffuse sound fields, the incident angle dependence of surface impedance has considerable influence on the resulting sound field, as presented by Yasuda et al. [12]. Using a non-diffused sound field with unevenly distributed absorbers, they showed the difference between extended and local reactions for a porous material layer with a rigid wall [12]. In addition, the example can confirm the inappropriateness of using diffuse field theory such as Sabine

and Eyring formulas. The inappropriateness is also shown briefly.

5.1. Setup of FE analysis

For calculations using the present FE solver with the extended reacting model of MPP absorbers, the setup of FE analyses is the same as that in Section 4.2, except in analyzed frequency ranges for transient responses. For the calculation of transient responses, frequencies of 50–1794 Hz were analyzed with a 0.5 Hz interval to satisfy the law of causality in inverse Fourier transform. The frequency interval was ascertained from the reverberation times estimated using the Eyring formula for the case without MPP. FE model was re-created for analyses with the surface impedance model in which a rigid backed air cavity was removed because the effect is treated by the surface impedance. Figure 12 presents the FE model. The surface impedance of the single-leaf MPP absorber with 0.1 m rigid backed air cavity was calculated using the electro-acoustical equivalent circuit theory [15]. The difference of absorption characteristics between the extended reacting and surface impedance models is discussed theoretically in the next subsection. The FE mesh was created to satisfy the spatial resolution of 4.9 elements per wavelength at 1414 Hz; the resulting DOFs of FE mesh are 840,000. The DOFs are slightly fewer than in the extended reacting model because of the removed air cavity, which is one advantage of a surface impedance model. The other settings are the same as those used in the extended reacting model.

5.2. Difference of absorption characteristics between the extended reacting model and surface impedance model

A single-leaf MPP absorber consists of an MPP and a rigid backed air cavity. MPP is assumed as limp in this paper. The acoustic impedance of MPP itself is independent of the incident angles of a plane wave. A sound wave propagates at the same angle as incident wave in the air cavity. The acoustic impedance of a rigid backed air cavity depends on incident angles, i.e., non-locally reacting air cavity. Consequently, the surface impedance of a single-leaf MPP absorber has incident angle dependence. The presented FE solver can analyze this dependence appropriately because it models a rigid backed air cavity directly. However, the surface impedance model based on a locally reacting assumption assumes that a sound wave propagates only perpendicularly to MPP surfaces in the air cavity, irrespective of the incident angle. Therefore, the acoustic impedance of air cavity is independent of the incident angle, i.e., a locally reacting air cavity. This is true also for the

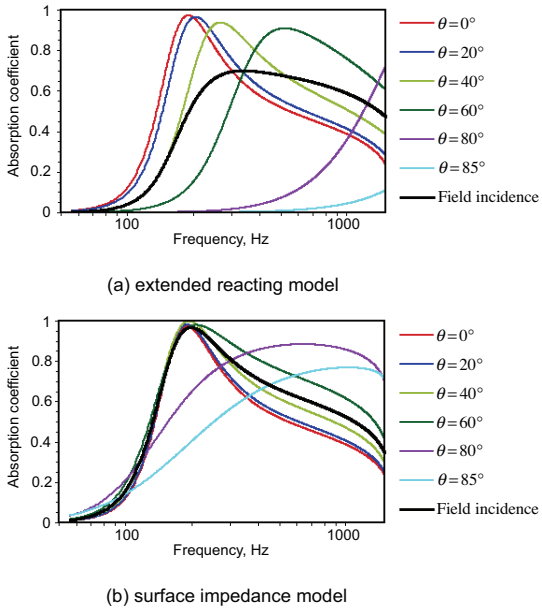

Figure 13: Oblique incidence absorption coefficient of (a) the extended reacting model and (b) the surface impedance model.

surface impedance of the absorber in the surface impedance model. For instance, a partitioned air cavity using a honeycomb structure might act as a locally reacting air cavity. The difference of absorption characteristics with non-locally and locally reacting air cavities is shown mathematically below.

For a limp single-leaf MPP absorber with a rigid backed air cavity, the surface impedance with the non-locally and locally reacting air cavities are given as

$$z_{\mathrm{n}} = \left(\frac{\rho_0 c_0}{Z_{\mathrm{MPP}}} + \frac{\rho_0 c_0}{i\omega M_{\mathrm{MPP}}}\right)^{-1} + z_{\mathrm{cavity}}, \tag{21}$$

where z_{cavity} is the normalized acoustic impedance of a rigid backed air cavity, and where z_{cavity} for the non-locally and locally reacting air cavity are represented respectively as

$$z_{\mathrm{cavity}} = \begin{cases} -\frac{i}{\cos\theta}\cot(kL\cos\theta) & (\text{non–locally reacting air cavity}), \\ -i\cot(kL) & (\text{locally reacting air cavity}). \end{cases} \tag{22}$$

Here, L represents the air cavity length. The oblique incidence absorption

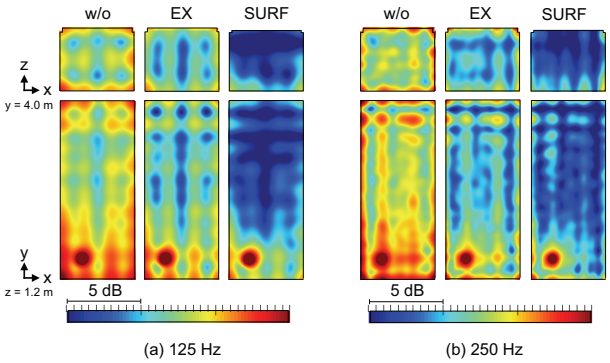

Figure 14: Oct. band SPL distributions at low frequencies (a) 125 Hz and (b) 250 Hz, in which the upper panel shows the distributions in a z–x plane at y = 4.0 m; the lower panel shows the x–y plane at z = 1.2 m. Symbols represent the following: w/o, the case without MPP; EX, the case with the extended reacting model; SURF, the case with the surface impedance model.

coefficient is calculated as

$$\alpha_\theta = \frac{4\mathrm{Re}[z_\mathrm{n}]\cos\theta}{(\mathrm{Re}[z_\mathrm{n}]\cos\theta + 1)^2 + (\mathrm{Im}[z_\mathrm{n}]\cos\theta)^2}. \tag{23}$$

Figures 13(a) and 13(b) respectively present the oblique incidence absorption coefficients of the single-leaf MPP absorber treated in the FE analyses for the extended reacting and surface impedance models. Here, the corresponding field incidence absorption coefficients are also presented, as calculated using Paris' formula. For the extended reacting model, a peak value in the absorption coefficient shifts to higher frequencies with larger incident angles. Furthermore, as important characteristics, grazing incidence waves are not absorbed at the low frequencies. In the surface impedance model, the incident angle dependence of the absorption coefficient is weaker than that in the extended reacting model. A peak in the absorption coefficient appears at almost identical frequency around 200 Hz except for the grazing incidence waves. In addition, a certain level of absorption is observed from the low frequencies for the grazing incidence waves. These results indicate that the incident angle dependence of surface impedance cannot be neglected when modeling a single-leaf MPP absorber. Moreover, greater difference between the extended reacting and surface impedance models is expected at lower frequencies in the subsequent numerical results.

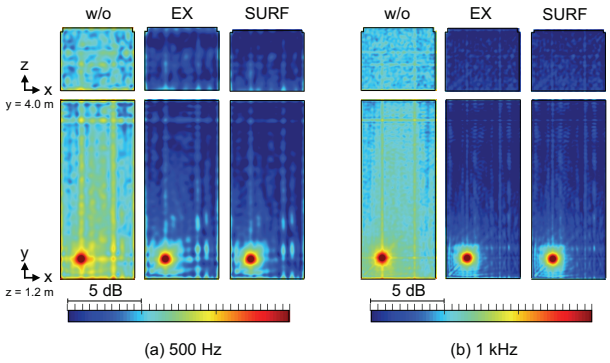

Figure 15: Oct. band SPL distributions at medium frequencies (a) 500 Hz and (b) 1 kHz, in which the upper panel shows the distributions in a z–x plane at y = 4.0 m; the lower panel shows the x–y plane at z = 1.2 m. Symbols represent the following: w/o, the case without MPP; EX, the case with the extended reacting model; SURF, the case with the surface impedance model.

5.3. Results and discussion

5.3.1. Comparison in a steady state sound field

Figures 14(a) and 14(b) show octave band SPL distributions at low frequencies, where symbols w/o, EX, and SURF respectively represent results for the case without MPP, the cases with extended reacting and surface impedance models. At both frequency bands, SPL reductions by installing the MPP absorber can be found for both the EX and SURF, but large differences are observed between them. The SPL reductions of SURF are greater than those of EX, which is expected because the oblique incidence absorption coefficient of SURF exhibits larger values at all incidence angles. Quantitatively, the SPL reductions in the EX are, respectively, 1.9 dB and 3.5 dB at 125 Hz and 250 Hz, as calculated using mean SPL over the 12 receiving points. Reductions for SURF are 5.9 dB and 5.5 dB. For SURF, a larger absorption effect can be found near the ceiling compared to the lower side in the z–x plane. The axial wave in the x direction dominates in the SPL distributions of EX, especially for 125 Hz, whereas axial waves in the z direction are absorbed because the absorber has the highest absorption coefficient for normal incidence, as portrayed in Fig. 13(a).

The octave band SPL distributions for mid-frequencies are portrayed in Figs. 15(a) and 15(b). The absorption effect by MPP absorber can be found in both EX and SURF. At 500 Hz, the absorption effect is greater for the SURF, although no distinct difference can be found at 1 kHz in the SPL

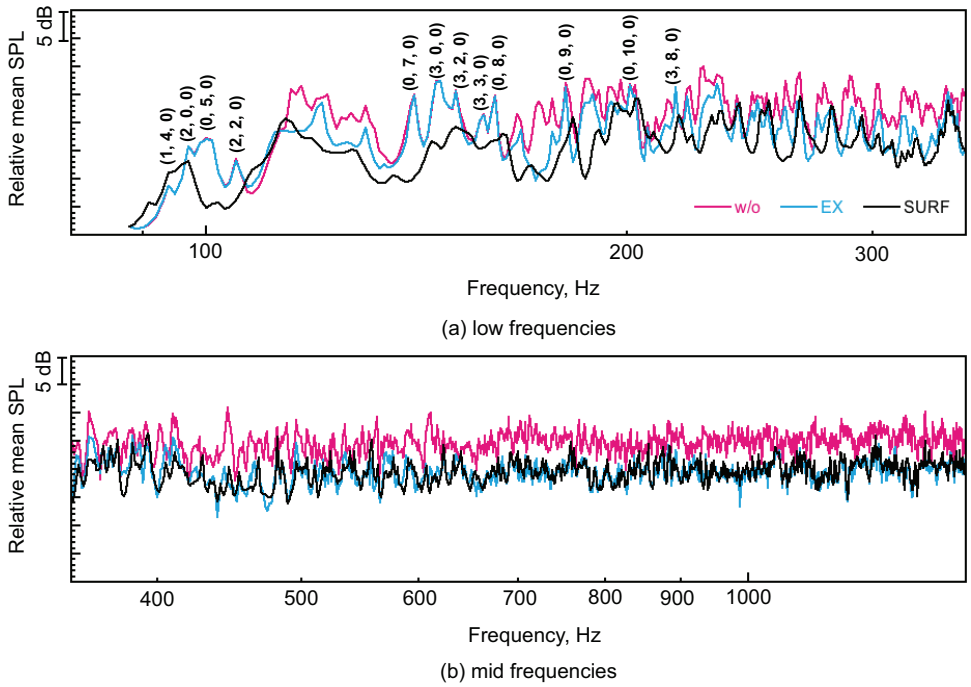

Figure 16: Frequency responses at (a) low and (b) medium frequencies. Symbols denote the following: w/o, the case without MPP; EX, the case with extended reacting model; SURF, the case with surface impedance model.

distributions between EX and SURF. Furthermore, the absorption near the ceiling is greater than at the lower sides of rooms for both EX and SURF, where no distinct axial wave in the x direction are visible. The SURF shows greater absorption until the lower side in the z–x plane, which might drive from the higher absorption coefficient for grazing incidence waves. However, in the lower side of room, the axial wave still dominates for both EX and SURF. This is visible also at 1 kHz. SPL reductions compared to the case without MPP are 4.8 dB (500 Hz) and 5.5 dB (1 kHz) for the EX, and 5.3 dB (500 Hz) and 5.1 dB (1 kHz) for the SURF.

For more detailed comparison between EX and SURF, frequency responses at the low frequencies and medium frequencies are presented respectively in Figures 16(a) and 16(b). The frequency responses are a mean value measured over the 12 receiving points R1–R12. At the low frequencies, as might be apparent in the SPL distributions, large differences can be found between EX and SURF. At almost all frequencies, SURF shows absorption

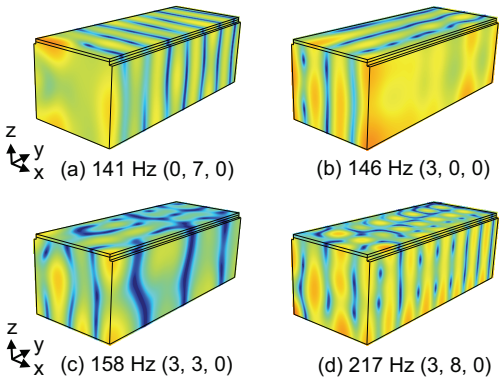

Figure 17: Examples of SPL distributions at frequencies with no absorption effect in the EX results: (a) 141 Hz, y–axial mode (0, 7, 0); (b) 146 Hz, x–axial mode (3, 0, 0); (c) 158 Hz, x–y plane tangential mode (3, 3, 0); and (d) 217 Hz, x–y plane tangential mode (3, 8, 0).

effect, although EX has frequencies with no absorption effect, especially at 125 Hz. We checked the mode shape in the frequencies with no absorption effect. Their mode indices are presented in Fig. 16(a). They were axial modes in the x and y directions and tangential mode in the x–y plane. In the modes, sound waves propagate parallel to the absorber surfaces. The single-leaf MPP absorber does not absorb such a grazing incidence waves at low frequencies, as portrayed in Fig. 13(a). Figure 17 presents examples of mode shape in the EX for the some frequencies. This ineffective absorption of a single-leaf MPP absorber in axial and tangential modes with a grazing incidence corresponds to findings reported by Liu and Herrin [24]. They presented its ineffectiveness in a small enclosure. We also confirmed that fact for this practical sized rectangular room with reflective surfaces, which further supports the reliability of present extended reacting model. Conversely, SURF shows absorption effects in the axial and tangential modes with a grazing incidence because it has a certain level of absorption for the grazing incidence waves at the low frequencies, as might be apparent in Fig. 13(b). This absorption is the main source of error related to the difference between EX and SURF at the low frequencies. The difference between EX and SURF is small at the medium frequencies, and especially at 1 kHz. In the frequency response, frequencies with no absorption effect are not readily apparent in the EX results. The extended reacting model has a certain level of absorption at larger incident angles for higher frequencies and higher

frequency ranges have high modal density. Therefore, these might be the reasons. The results clearly confirmed the importance of dealing with the incident angle dependence of surface impedance. The surface impedance model shows large errors for grazing incidence waves at low frequencies attributable to the higher grazing incidence absorption.

5.3.2. Comparison in transient sound field

First, 1/3 octave band limited impulse responses were calculated at the 12 receiving points using the inverse Fourier transform of the frequency responses with IIR bandpass filtering. From them, reverberation times were calculated further. Figure 18 presents the reverberation times at the 1/3 octave band obtained using FEM (EX), FEM (SURF), and the Eyring formula for the case with MPP. FEM (w/o) is also shown. Here, FEM (EX) and FEM (SURF) respectively represent FEM values with the extended reacting and surface impedance models. Compared to FEM (EX), Eyring values underestimate at all frequencies. FEM (EX) values are almost identical to those obtained in the case without MPP. i.e., FEM (w/o). Similarly, FEM (SURF) has almost identical values to those obtained using FEM (w/o) at the mid-frequencies, but it has lower values at the low frequencies. In other words, FEM (EX) and FEM (SURF) show a difference only at the low frequencies. To confirm the respective decay processes, reverberation decay curves at a receiving point R4 are presented in Fig. 19. Compared to the ideal reverberation decay by the Eyring formula, FEM (EX) shows markedly slower decays at all frequencies. This sound field has a reflective floor and side walls. The single-leaf MPP ceiling absorber has low grazing incidence absorption coefficients. Therefore, this slow decay of FEM (EX) results from the slower decay of axial and tangential modes in horizontal directions. Clear domination of the axial mode in the x direction is apparent in the SPL distributions in Figs. 14 and 15. It is out of the application range of the Eyring formula. FEM (SURF) shows faster decay at 125 Hz and slower decay at frequencies higher than 250 Hz. The faster decay at 125 Hz results from the greater absorption at all incidence angles in the surface impedance model, as presented in Fig. 13(b). The slower decay is also attributable to the slower decay of axial and tangential modes in the horizontal directions. Although the surface impedance model has a high absorption coefficient for the grazing incidence waves at the mid-frequencies, it is readily apparent that the axial mode in the x direction remains in the lower sides of rooms, as presented in Fig. 15, whereas the axial mode is more attenuated near the absorbers. Results con-

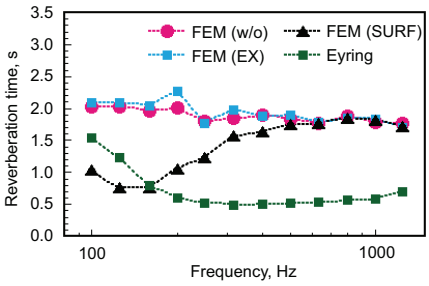

Figure 18: Reverberation times obtained using FEM (EX and SURF) and the Eyring formula for the case with MPP; FEM (w/o) is also shown for reference.

firmed that the inappropriate treatment of the incidence angle dependence in surface impedance engenders markedly different reverberation decay at low frequencies.

5.3.3. Additional analysis

As an additional analysis, this section briefly demonstrates that the present FE solver can model multiple MPP absorbers. This is achieved by imposing the boundary condition of Eq. (1) for respective MPP absorbers. For the purpose, a single-leaf MPP wall absorber was further installed to the rectangular room with MPP ceiling absorber of Fig. 7. Figure 20 shows the analyzed rectangular room, in which MPP elements of Case A in Fig. 1 were used to model the MPP wall absorber. The backing cavity depth and material properties of wall absorber are the same as the ceiling absorber. The frequency response at 125 Hz ranges was analyzed with 1 Hz interval. The DOF of FE mesh is 887,250, in which 10,788 MPP FEs were used to model the MPP wall absorbers. Figure 21 shows a comparison of frequency response at 125 Hz for the cases with ceiling absorber and ceiling + wall absorbers. For the case with MPP ceiling and wall absorbers, as expected, the axial modes in y-direction are still dominant because of the ineffective absorption of single-leaf MPP absorber for grazing incidence waves, whereas the tangential modes in x–y plane are absorbed effectively by the wall absorber. This can be also observed in octave band SPL distribution in Fig. 22. As in the presented case, the present formulation can be modeled multiple MPP absorbers easily.

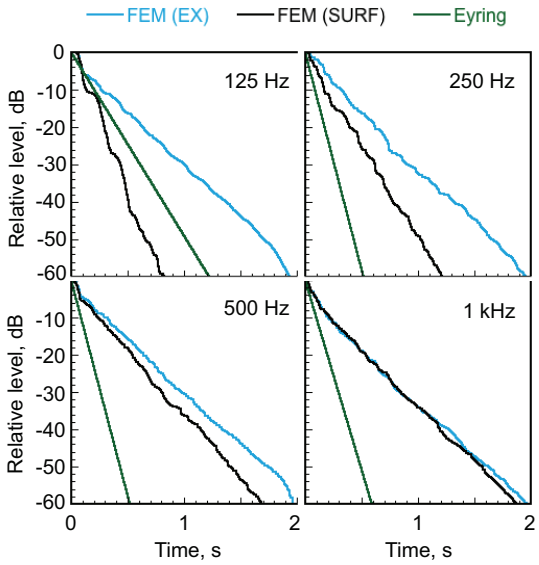

Figure 19: Reverberation decay curves at R4 obtained using FEM (EX and SURF) and the Eyring formula for the case with MPP.

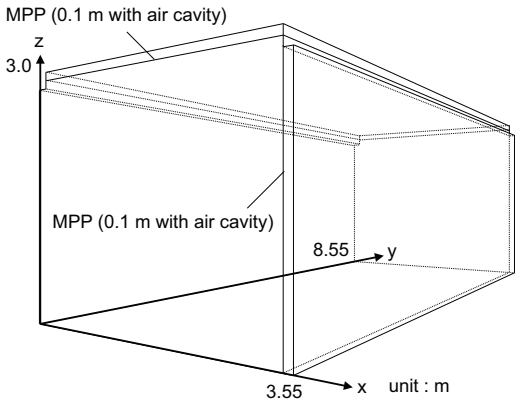

Figure 20: A simulated room with single-leaf MPP ceiling and wall absorbers. MPP elements in Case A are used to model MPP wall absorber.

6. Conclusions

This paper presents development of frequency domain finite element solvers for acoustics simulations of 3D rooms with MPP absorbers, which uses the fourth-order accurate hexahedral FEs with MIR for spatial discretization, and first-order limp hexahedral MPP element for dealing with sound wave

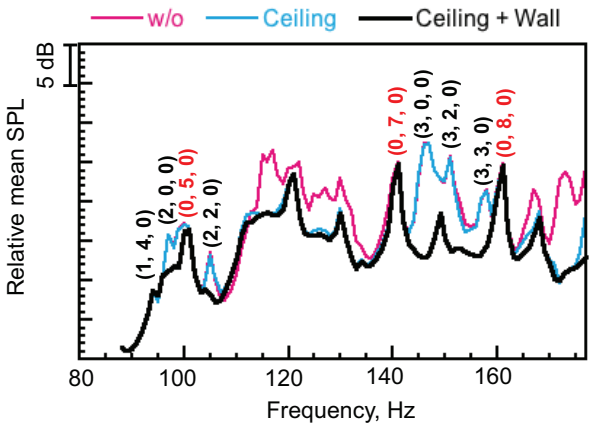

Figure 21: Comparison of frequency responses at 125 Hz for the cases with ceiling absorber and with ceiling + wall absorbers. The case without absorber (w/o) is also shown for reference.

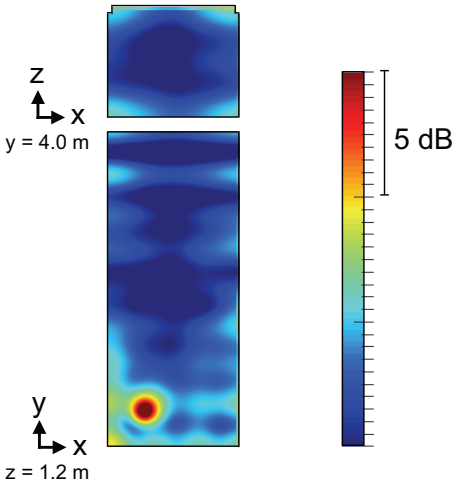

Figure 22: Oct. band SPL distributions at 125 Hz for the case with MPP ceiling and wall absorbers.

propagation in backing structures of MPP absorbers. An iterative solver for efficient multi-frequency analyses is also presented. Impedance tube problems using three FE meshes with different spatial resolutions show that the solutions of present FE solver converge to theoretical values with the finer mesh. The superiority of using MIR is also confirmed in comparison with the conventional second-order accurate hexahedral FEs. CSQMOR itera-

tive solver is found to be effective for solving the linear system of equations at each frequency, with faster convergence and smoother residual reduction. The efficiency is enhanced especially at higher frequencies. Finally, the effectiveness of present FE solver is confirmed through the example calculation. The calculation shows that neglecting the incident angle dependence of surface impedance attributable to a non-locally reacting rigid backed air cavity engenders considerable error in the resulting sound fields. In future reports, details of the absorption performance of MPP absorbers in room acoustic applications will be presented using the present FE solver.

Acknowledgments

This work was supported in part by JSPS KAKENHI Grant No. 15K18167. The computation was partly conducted using the computer facilities at the Research Institute for Information Technology, Kyushu University.

References

[1] Maa DY. Microperforated-panel wideband absorbers. Noise Control Eng J 1987;29(3):77–84.

[2] Maa DY. Potential of microperforated panel absorber. J Acoust Soc Am 1998;104(5):2861–66.

[3] Sakagami K, Morimoto M, Koike W. A numerical study of double-leaf microperforated panel absorbers. Appl Acoust 2006;67:609–19.

[4] Sakagami K, Nagayama Y, Morimoto M, Yairi M. Pilot study of wideband sound absorber obtained by combination of two different microperforated panel (MPP) absorbers. Acoust Sci and Tech 2009;30(2):154–6.

[5] Sakagami K, Yairi M, Morimoto M. Multiple-leaf sound absorbers with microperfrated panels: An overview. Acoust Australia 2010;38(2):76–81.

[6] Sakagami K, Nakamori T, Morimoto M, Yairi M. Absorption characteristics of a space absorber using a microperforated panel and a permeable membrane. Acoust Sci and Tech 2011;32(1):47–9.

[7] Yairi M, Sakagami K, Takebayashi T, Morimoto M. Excess sound absorption at normal incidence by two microperforated panel absorbers with different impedance. Acoust Sci and Tech 2011;32(5):194–200.

[8] Wang C, Huang L. On the acoustic properties of parallel arrangement of multiple micro-perforated panel absorbers with different cavity depths. J Acoust Soc Am 2011;130(1):208–18.

[9] Bistafa SR, Bradley JS. Predicting reverberation times in a simulated classroom. J Acoust Soc Am 2000;108(4):1721–31.

[10] Yasuda Y, Ushiyama A, Sakamoto S, Tachibana H. Experimental and numerical studies of reverberation characteristics in a rectangular room with unevenly distributed absorbers. Acoust Sci and Tech 2006;27(6):366–74.

[11] Okuzono T, Sakagami K. A finite-element formulation for room acoustics simulation with microperforated panel sound absorbing structures:Verification with electro-acoustical equivalent circuit theory and wave theory. Appl Acoust 2015;95:20–6.

[12] Yasuda Y, Ueno S, Kadota M, Sekine H. Applicability of locally reacting boundary conditions to porous material layer backed by rigid wall: Wave-based numerical study in non-diffuse sound field with unevenly distributed sound absorbing surfaces. Appl Acoust 2016;113:45–57.

[13] Okuzono T, Sakagami K. Room acoustics simulation with single-leaf microperforated panel absorber using two-dimensional finite-element method. Acoust Sci and Tech 2015;36(4):358–61.

[14] Guddati MN, Yue B. Modified integration rules for reducing dispersion error in finite element methods. Comput Methods Appl Mech Engrg 2004;193:275–87.

[15] Sakagami K, Morimoto M, Yairi M. A note on the effect of vibration of a microperforated panel on its sound absorption characteristics. Acoust Sci and Tech 2005;26(2):204–7.

[16] Okamoto N, Tomiku R, Otsuru T, Yasuda Y. Numerical analysis of large-scale sound fields using iterative methods Part II: Application of Krylov subspace methods to finite element analysis. J Comp Acous 2007;15(4):473–93.

[17] van der Vorst HA, Melissen J. A Petrov–Galerkin type method for solving $Ax=b$, where A is symmetric complex. IEEE Trans Magn 1990;26(2):706–8.

[18] Sonneveld P. A fast Lanczos-type solver for nonsymmetric linear system. SIAM J Sci Stat Comput 1989;10:36–52.

[19] van der Vorst HA. Bi-CGStab: a fast and smoothly converging variant of Bi-CG for the solution of nonsymmetric linear system. SIAM J Sci Stat Comput 1992;13:631–44.

[20] Zhang SL. GPBi-CG: generalized product-type methods based on Bi-CG for solving nonsymmetric linear system. SIAM J Sci Stat Comput 1997;18:537–51.

[21] Freund RW, Nachtigal NM. An implementation of the QMR method based on coupled two-term recurrences. SIAM J Sci Stat Comput 1994;15(2):313–37.

[22] Sogabe T, Zhang SL. A COCR method for solving complex symmetric linear systems. J Comput Appl Math 2007;199:297–303.

[23] Zhang J, Dai H. A new quasi-minimal residual method based on a bi-conjugate A-orthonormalization procedure and coupled two-term recurrences. Numer Algor 2015;70:875–896.

[24] Liu J, Herrin DW. Enhancing micro-perforated panel attenuation by partitioning the adjoining cavity. Appl Acoust 2010;71:120–7.